72 Vol. 2, No. 2 / 25 April 2024 / Optica Quantum Research Article

OPTICA QUANTUM

Traceable localization enables accurate integration of quantum emitters and photonic structures with high yield

Craig R. Copeland,[1] Adam L. Pintar,[2] Ronald G. Dixson,[1] Ashish Chanana,[1] Kartik Srinivasan,[1,3] Daron A. Westly,[1] B. Robert Ilic,[1,4] Marcelo I. Davanco,[1] and Samuel M. Stavis[1,*]

[1]Microsystems and Nanotechnology Division, National Institute of Standards and Technology, Gaithersburg, Maryland 20899, USA
[2]Statistical Engineering Division, National Institute of Standards and Technology, Gaithersburg, Maryland 20899, USA
[3]Joint Quantum Institute, NIST/University of Maryland, College Park, Maryland 20742, USA
[4]CNST NanoFab, National Institute of Standards and Technology, Gaithersburg, Maryland 20899, USA
*samuel.stavis@nist.gov

Received 8 August 2023; revised 22 December 2023; accepted 2 January 2024; published 18 March 2024

In a popular integration process for quantum information technologies, localization microscopy of quantum emitters guides lithographic placement of photonic structures. However, a complex coupling of microscopy and lithography errors degrades registration accuracy, severely limiting device performance and process yield. We introduce a methodology to solve this widespread but poorly understood problem. A new foundation of traceable localization enables rapid characterization of lithographic standards and comprehensive calibration of cryogenic microscopes, revealing and correcting latent systematic effects. Of particular concern, we discover that scale factor deviation and complex optical distortion couple to dominate registration errors. These novel results parameterize a process model for integrating quantum dots and bullseye resonators, predicting higher yield by orders of magnitude, depending on the Purcell factor threshold as a quantum performance metric. Our foundational methodology is a key enabler of the lab-to-fab transition of quantum information technologies and has broader implications to cryogenic and correlative microscopy.

https://doi.org/10.1364/OPTICAQ.502464

1. INTRODUCTION

Localization microscopy has left the diffraction limit of a few hundred nanometers in the rear-view optics, enabling nanoscale measurements in diverse microsystems ranging from biological imaging to photonic integration [1–3]. As localization methods mature, reproducibility concerns deepen [4,5], and demanding applications emerge [6–10], a better understanding of total uncertainty becomes necessary. Whereas the random effect of shot noise from a finite count of signal photons can be less than one nanometer [11–13], systematic effects can be orders of magnitude larger and vary unpredictably across an imaging field [13]. Identification and correction of systematic effects requires comprehensive calibration of optical microscopes [13–16], which is uncommon, leading to a common discrepancy of precision and accuracy, and potential overconfidence in localization data. Moreover, no previous study has established a calibration chain with localization uncertainty that is reliably traceable to the International System of Units (SI). The traceability of localization data is much more than a formality and is indeed a requirement to extract reliable quantities from optical micrographs. Specifically, a traceable calibration allows the transformation of erroneous positions in pixel units to accurate positions in SI units of nanometers, creating absolute position data for dependent applications.

A calibration can be only as good as the standard providing a reference. Unofficial standards for applications of localization microscopy to biological imaging include fluorescent particles for calibration of point spread functions and registration of data at different wavelengths [15,17,18], molecular nanostructures for calibration of local scale factors [19,20], and nanoscale apertures for all these calibrations, as well as global calibrations of the imaging field and stability tests [13,21]. Of these unofficial standards, aperture arrays are relatively uncommon but feature flexibility of design from the top down and use under different imaging conditions, accessibility for correlative microscopy to establish traceability, and experimental stability and reusability [13,21]. Lithographic standards are more common in applications of localization microscopy to the integration of quantum emitters and photonic structures. In particular, electron-beam lithography enables fabrication of fiducial structures of several types. In addition to alignment marks, such features can provide reference positions to register emitter positions, calibrate scale factors, and correct aberration effects in optical microscopes [6,7,22–26].

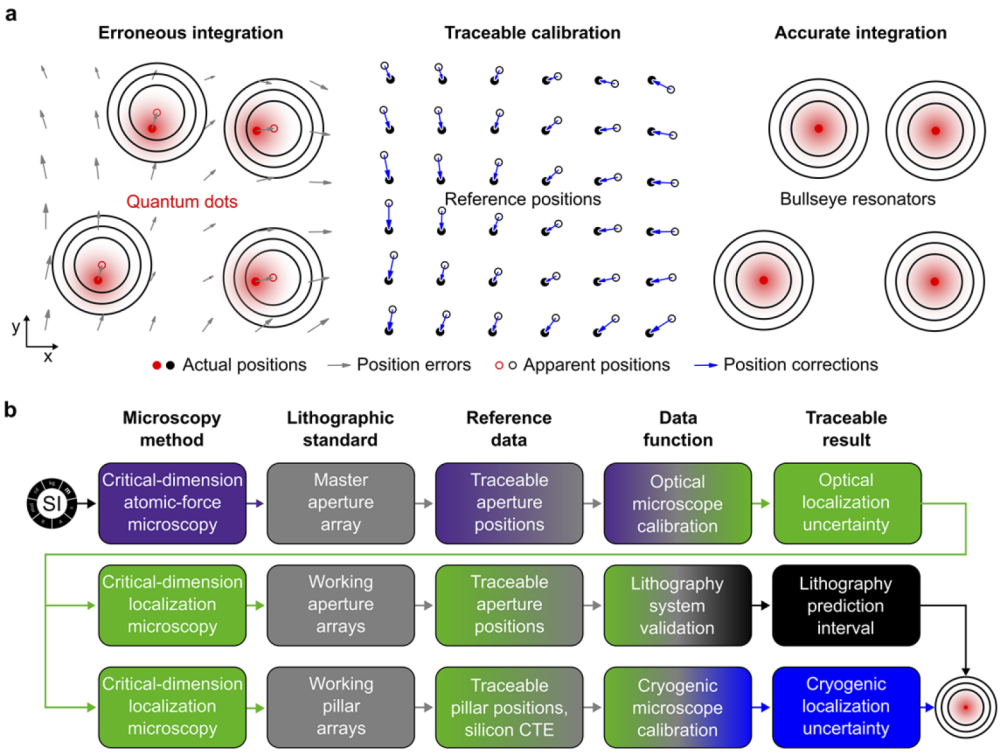

Fig. 1. Overview. (a) Schematic showing the integration of quantum dots and bullseye resonators. (Left) Erroneous integration decreases process yield. (Center) Traceable calibration improves integration accuracy. (Right) Accurate integration increases process yield. (b) Schematic showing a traceability chain from SI units of nanometers to the accurate integration of a quantum dot and a bullseye resonator. Monocolor boxes map colors to topics. Multicolor boxes indicate the combination of multiple topics. CTE is the coefficient of thermal expansion.

Even with a standard in hand or on chip, four challenges impede traceable localization. The first challenge is matching all conditions—system optics, imaging modes, sample positions, and localization analyses—between calibration and experiment [13]. Any inconsistency can degrade accuracy and compromise reliability, such as by limiting the applicability of calibration data that diverge from the experimental context of localization microscopy [20,27,28]. This issue compounds the second challenge of calibrating the scale factor, or mean magnification, or image pixel size of an optical microscope with low uncertainty. These limits pertain to the third challenge of sampling the imaging field with structures that are suitable for localization microscopy and that probe field non-uniformity at the scale from one to ten wavelengths [13,15]. The fourth challenge is maintaining the integrity of the calibration chain by quantitating uncertainty and validating results. No previous study has met all these challenges, and no application would benefit more from meeting these challenges than the widefield integration of quantum emitters and photonic structures to develop quantum information technologies.

At the state of the art, such integration processes generally require emitter localization to guide structure placement [10], with optimal coupling occurring within a registration error of a few tens of nanometers [6,26,29,30]. In a canonical example, epitaxial growth self-assembles quantum dots at random positions in semiconductor substrates, requiring localization to place bullseye resonators that yield single-photon sources. Emitter positions are possible to measure by several methods, including scanning confocal microscopy [31,32] and cathodoluminescence microscopy [33]. Yet, no method achieves higher throughput with simpler instrumentation than widefield imaging [6,7,22–26,34,35], in conjunction with a sample cryostat to enable the operation and measurement of quantum emitters, and electron-beam lithography of fiducial structures and photonic structures. However, localization and placement errors degrade registration accuracy across a wide field [Fig. 1(a)]. No previous study has rigorously investigated these systematic effects, which can severely limit process yield.

Improving accuracy is, therefore, a topic of interest. Previous studies have reduced errors due to barrel distortion [26], reduced aberration effects by a perspective transformation [7], and improved localization of alignment marks by avoiding laser misalignment [24]. In addition, a review noted two issues—the common assumption of lithographic accuracy and the potential utility of our microscope calibration [10]. The coupling of these issues is problematic and poorly understood. In essence, accurate lithographic standards are necessary for optical microscope calibration, but a calibrated optical microscope is necessary to assess and guide accurate lithography [Fig. 1(b)]. For the registration of absolute position data across microscopy and lithography systems with unrecognized errors and nonobvious interactions, the coupled problem is highly complex. For example, an inaccurate lithographic standard contracts in a cryogenic localization microscope, coupling scale factor deviations that erroneously expand or contract widefield position data. Simultaneously, complex optical distortion causes irregular localization errors of fiducial structures further corrupting scale factor calibration, and of quantum emitters subsequently misguiding lithographic placement of photonic structures. Decoupling and addressing such issues is the key to unlocking high performance and yield.

In the present study, a new foundation of traceable localization enables lithographic process characterization and cryogenic microscope calibration [Fig. 1(b)], revealing, correcting, and decoupling errors that limit this popular integration process. We begin by creating a master standard, leading to the concept of an uncertainty field with subnanometer regions. Traceable localization enables metrology of working standards with high throughput, facilitating characterization of lithographic scale factor. The results validate subnanometer accuracy on average but reveal larger distributional deviations. Applying our methods to calibrate cryogenic microscopes, we introduce working standards in silicon with a crystallographic orientation of (100) as a reference material. The results elucidate additional sources of scale factor deviation, as well as the critical issue of complex optical distortion. The coupling of these systematic effects, among others, can dominate the random effect of photon shot noise, causing erroneous registration of quantum emitters and photonic structures. Integrating all these results, we parameterize a comprehensive model of registration errors between quantum dots and bullseye resonators. The model predicts higher yield by up to two orders of magnitude relative to previous studies, depending on Purcell factor threshold as a quantum performance metric.

Beyond this specific example, our methodology is generally useful for integrating quantum emitters and photonic structures to develop quantum information technologies [6,7,24,29,30,36], and beyond this field of research, our standards and calibrations are generally applicable to improve accuracy and achieve traceability in microscope systems. The implications of our work extend directly to correlative electron and photon microscopy for biological imaging [5,37–42], potentially with better precision at cryogenic temperatures [43–45] but typically without supporting accuracy. Other demanding applications such as nanoparticle characterization [46], microsystem tracking [15], and semiconductor metrology [47] could also benefit.

2. RESULTS AND DISCUSSION

In a previous study, we fabricated aperture arrays by electron-beam lithography and tested aperture placement [13]. Two lithography systems each used two interferometers to control stage positions and correct for electron-optical aberrations within the patterning process. By localizing apertures and comparing placements by the two systems, we estimated a mean distance between apertures that differed by one part in five thousand, or approximately 1 nm, as well as random placement errors of approximately 2 nm. Although the implication was placement accuracy at the nanometer scale, these test results were insufficient to claim traceability. Moreover, the significant difference of mean distance raises questions about the variability of our lithography process to set critical dimensions for demanding applications.

To address these issues, which are fundamental to the accuracy of standards and the reliability of calibrations, we selected one of the aperture arrays from our previous test [13] for traceable metrology. We presently image 21 pairs of adjacent apertures in triplicate, and one pair in duplicate, by critical-dimension atomic-force microscopy [Figs. 2(a) and 2(b), Tables 1 and S1]. The two axes of the atomic-force microscope scan independently and are nominally orthogonal, which we test subsequently. Each axis probes the aperture sidewalls with a flared tip, measuring the distance between 11 different pairs of apertures with a resolution of less than 0.1 nm and a relative uncertainty of approximately one part in ten thousand [48–51]. We report all uncertainties as 68% coverage intervals (Note S1, Table S2) [52–56]. This relative uncertainty of 10^{-4} results from calibration of mean scale factor and correction of scanfield distortion [Fig. 3(a)], using a one-dimensional grating with a traceable pitch. We select for analysis sidewall positions ranging from 30 nm to 95 nm above the zero plane of the silica substrate (Fig. S1), assuming that this nearly vertical region determines the transmission of light through apertures in subsequent optical microscopy. A comparison of elliptical models and centroid analyses of the sidewall positions to localize each aperture yields consistent results. Least-squares fits of elliptical models with uniform weighting smooth the scatter of the sidewall positions, reducing the pooled standard deviation of the distance between pairs of adjacent apertures from 1.50 nm to 0.98 nm, so we proceed with this analysis.

Complementary statistical models enable analyses of the aperture pair distances, creating a master standard (Note S2, Table 1). Fixed-effect models for both atomic-force microscopy and optical microscopy assess localization accuracy and enable an interstudy comparison. An autoregressive model accounts for the correlation of adjacent aperture pairs in atomic-force microscopy [Fig. 2(a)], but the comparable results of the two models are similar. Accordingly, the fixed-effect model for atomic-force microscopy yields a mean distance of 5000.72 nm ± 0.24 nm for axis 1, 5000.69 nm ± 0.06 nm for axis 2, and 5000.71 nm ± 0.13 nm for both axes. These uncertainties account for variability from replicate measurements of the 22 pairs of apertures (Table S1). Propagation of scale factor uncertainty (Table S2) results in a traceable mean distance of 5000.71 nm ± 0.54 nm. Although this pitch of the master standard is near to the nominal value, subsequent tests of more standards are necessary to sample variation of the lithographic process, with important implications for setting critical dimensions.

We image the aperture array by optical microscopy using our previous methods [13], modifying the calibration to achieve traceability. We record 1000 replicate images of the entire array near best focus [Figs. 2(c)–2(e), Table S1]. A similarity transformation between an ideal array of positions in SI units of nanometers and the apparent positions resulting from localization analysis in units of pixels determines the mean magnification of the optical microscope, setting the scale factor in the form of an image pixel size. To achieve traceability, the mean distance between aperture pairs of the master standard from atomic-force microscopy, rather than the nominal pitch of the array from electron-beam lithography, defines the pitch of the ideal array. This calibration reveals that assuming the nominal magnification of the objective lens results in a scale factor error of 3.1% [13], causing egregious position errors [Fig. 3(b)]. We revisit scale factor errors due to reliance on an erroneous reference dimension. Position errors remain after the similarity transformation [Fig. 3(c)] due to widefield distortion and other aberration effects, which a Zernike polynomial model corrects [Fig. 3(d)] [13]. In another modification of our calibration, correlation of aperture distances between optical and atomic-force microscopy traceably optimizes the number of polynomial terms in the correction model. For 144 apertures in a field of 3600 μm^2, a Zernike model that includes all polynomials up to a Noll index of 41 for x and 48 for y minimizes root-mean-square deviations of distance between the same aperture pairs by the

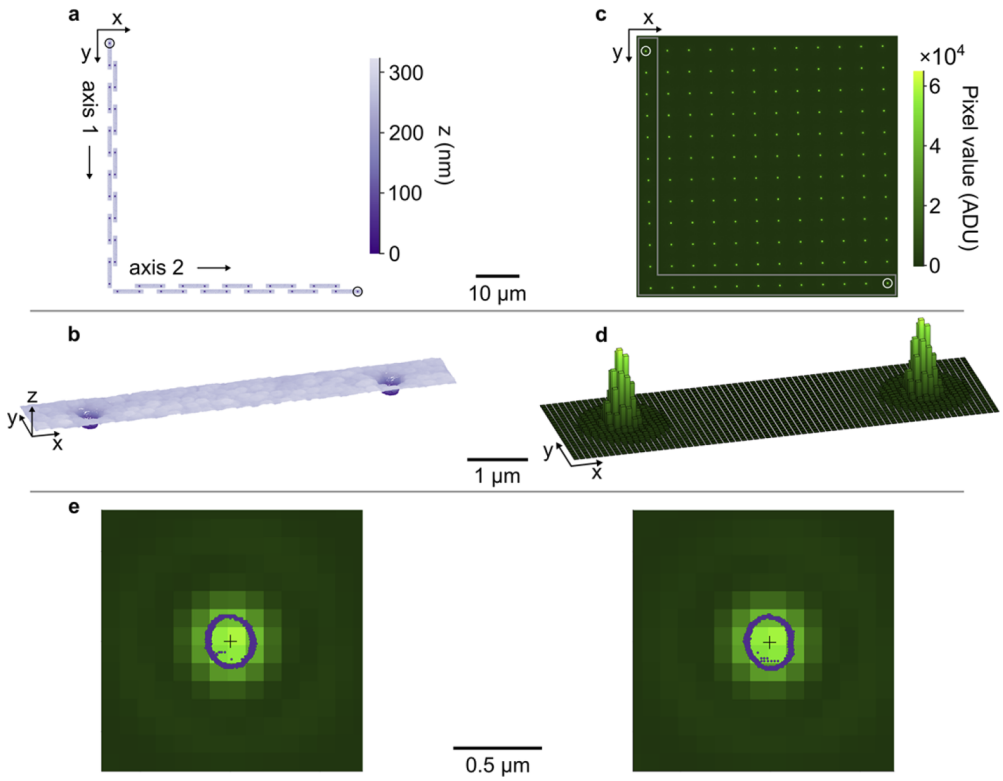

Fig. 2. Correlative microscopy. (a),(b) Atomic-force micrographs showing (a) separate images of the 22 pairs of apertures comprising the left column and bottom row of apertures in the array, and (b) an image of a representative pair of apertures. (c),(d) Optical micrographs showing (c) the entire aperture array and (d) an image of the same representative pair of apertures in (b). The gray outline in (c) indicates the same apertures as in (a). Circles in (a) and (c) indicate two corner apertures. (e) Correlative micrographs overlaying image data from the two microscopy methods for the aperture pair in (b),(d). Purple dots are the aperture sidewall data from atomic-force microscopy that we use to determine the aperture positions. Black crosses mark the positions resulting from both localization analyses. Position uncertainties are smaller than the cross linewidths.

two microscopy methods [Figs. 3(c) and 3(d)]. Importantly, both scale factor errors and optical distortion errors can be even more significant over larger imaging fields [13].

A comparison of aperture pair distances from the two microscopy methods manifests uncertainty components that are rich with information (Table 1, Note S2). The distances are in evident agreement and correlate to within a few nanometers (Fig. 4, Table S1), even as the feature sidewalls are an order of magnitude rougher [Figs. 2(e) and S1]. The distance deviations have a mean of zero within uncertainty (Table S1) and variances that enable determination of limiting uncertainty components for optical microscopy. In the fixed-effect models, the total variances are [Eq. (1)] $\sigma^2_{D^{\mathrm{AFM}}} = \sigma^2_{\delta^{\mathrm{AFM}}} + \sigma^2_{d^{\mathrm{AFM}}}/n_{D^{\mathrm{AFM}}}$ for atomic-force microscopy (AFM) and [Eq. (2)] $\sigma^2_{D^{\mathrm{OM}}} = \sigma^2_{\delta^{\mathrm{OM}}} + \sigma^2_{d^{\mathrm{OM}}}/n_{D^{\mathrm{OM}}}$ for optical microscopy (OM) (Note S2). We divide the variances from replicate measurements, $\sigma^2_{d^{\mathrm{OM}}}$ and $\sigma^2_{d^{\mathrm{AFM}}}$, by the sample sizes $n_{D^{\mathrm{AFM}}}$ and $n_{D^{\mathrm{OM}}}$, as we average distances over replicate measurements. The variances $\sigma^2_{\delta^{\mathrm{AFM}}}$ and $\sigma^2_{\delta^{\mathrm{OM}}}$ are from localization errors, such as from non-uniform scale or deviations of localization models from aperture images. For optical microscopy, $\sigma_{d^{\mathrm{OM}}}/\sqrt{2}$ is the empirical localization precision and $\sigma^2_{\delta^{\mathrm{OM}}}/2$ is the variance of position from errors that are unobservable in replicate measurements (Table S3) [13]. Assuming independence of random effects, the sample variance of the distance deviations is the sum of Eq. (1) and Eq. (2): $\sigma^2_{D^{\mathrm{OM}}-D^{\mathrm{AFM}}} = \sigma^2_{\delta^{\mathrm{OM}}} + \sigma^2_{d^{\mathrm{OM}}}/n_{D^{\mathrm{OM}}} + \sigma^2_{\delta^{\mathrm{AFM}}} + \sigma^2_{d^{\mathrm{AFM}}}/n_{D^{\mathrm{AFM}}}$ [Eq. (3)]. Pooling the sample variances of the replicate measurements over all aperture pairs yields values for $\sigma^2_{d^{\mathrm{AFM}}}$ and $\sigma^2_{d^{\mathrm{OM}}}$, separately for each axis of the atomic-force microscope, due to the higher variability of axis 1 from a control algorithm to improve sidewall tracking (Fig. 4). We estimate $\sigma^2_{\delta^{\mathrm{AFM}}}$ for each axis. For axis 1, the scale factor is nearly constant in the region of interest [Fig. 3(a)], yielding a negligible value of $\sigma_{\delta^{\mathrm{AFM}}}$ (Table 2). For axis 2, the scale factor varies nearly linearly in the region of interest [Fig. 3(a)], and we use a scale factor correction from near the mid-point of the aperture pairs. The repeatability of sample positioning is within 0.2 μm, yielding a larger but still negligible value of $\sigma_{\delta^{\mathrm{AFM}}}$ for this axis (Table 2). For this reason, replication effects dominate the variance of atomic-force microscopy for both axes. For optical microscopy, averaging $n_{D^{\mathrm{OM}}} = 1000$ replicate measurements, with 0.6×10^6 signal photons per image, reduces $\sigma^2_{d^{\mathrm{OM}}}/n_{D^{\mathrm{OM}}}$ to a negligible value (Table S4) [57]. Having estimates of all other terms in Eq. (3), we solve for $\sigma^2_{\delta^{\mathrm{OM}}}$ (Tables 2 and S4).

The resulting estimate of optical localization error enables an interstudy validation and provides new insight into the nonuniformity of optical imaging fields. The quantities of $\sigma_{\delta^{\mathrm{OM}}}$, in both the x and y directions, agree within uncertainty with the corresponding quantities from our previous study with a larger imaging field of 40,000 μm^2 (Table 2) [13]. This agreement provides a consistency check for this optical microscope and further indicates that its limiting localization errors are spatially random and independent of field area. The effect of fabrication precision,

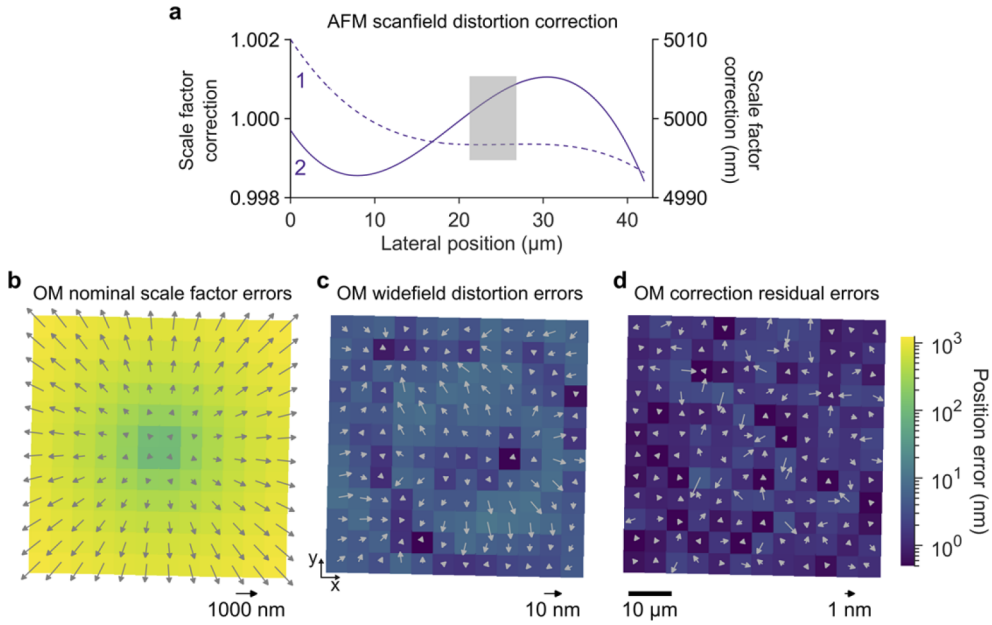

Fig. 3. Microscopy calibrations and corrections. (a) Plot showing scanfield distortion corrections for (dash line) axis 1 and (solid line) axis 2 of the atomic-force microscope. The gray box indicates the region of interest. (b)–(d) Vector plots and logarithmic color maps showing position errors for optical microscopy, (b) assuming the nominal scale factor or magnification of the system is accurate, (c) after calibration of mean scale factor, and (d) after scale factor calibration and widefield distortion correction. The optical calibration is insensitive to the evident rotation of the aperture array relative to the coordinate system of the imaging sensor. AFM is atomic-force microscopy. OM is optical microscopy.

or actual deviations of aperture positions from the lithographic design, on the Zernike polynomial model causes localization errors of less than 0.1 nm [13]. Wavefront errors that aberrate the imaging field at micrometer scales are a likely cause of the remaining optical localization errors. The subsequent calibration of a cryogenic microscope supports this likelihood, showing qualitatively similar but quantitatively larger localization errors.

Optical localization error sets a lower bound of traceable position uncertainty, but scale factor uncertainty becomes increasingly problematic across a wide field. This effect limits the accurate integration of quantum emitters and photonic structures, among other applications that require reliable registration of position data, such as correlative microscopy. To quantify this trend, $\sigma_{D^{\mathrm{OM}}}$ sums in quadrature with a scale factor uncertainty component. For the position uncertainty of a single point from localization analysis, relative to a reference point that requires no localization analysis, such as a pixel position, the values of $\sigma_{D^{\mathrm{OM}}}$ reduce by a factor of $\sqrt{2}$. The uncertainty is then [Eq. (4)] $u_{D_{\mathrm{x}}^{\mathrm{OM}}} \approx \sqrt{\left(\sigma_{D_{\mathrm{x}}^{\mathrm{OM}}}/\sqrt{2}\right)^2 + \left(D_{\mathrm{x}}^{\mathrm{OM}} \times \sigma_S\right)^2}$ (Fig. 5, Tables 2 and S2), where $D_{\mathrm{x}}^{\mathrm{OM}}$ is the distance in the x direction from a reference point, with an analogous expression for the y direction, and σ_S is the relative uncertainty of scale factor. A relative error of scale factor, ϵ_S, can exceed σ_S and yield a similar effect of greater magnitude [Fig. 3(b)] [13]. A general expression for the uncertainty of distance D^{OM}, including localization uncertainty for two points, is in Note S3. The first term in Eq. (4) is constant, whereas the second term scales with distance [Fig. 5(a)]. This trend is characteristic of coordinate-measuring machines, closing the gap between such systems and conventional optical microscopes. Equation (4) and its analog in the y direction describe an uncertainty field with two regions of positions with subnanometer traceability [Fig. 5(b)]. In the inner and outer regions, respectively, the maximum and mean uncertainty is less than ± 1.0 nm across areas of 180 μm^2 and 390 μm^2. The uncertainty field exhibits asymmetric variation around the center due to different values of $\sigma_{\delta_{\mathrm{x}}^{\mathrm{OM}}}$ and $\sigma_{\delta_{\mathrm{y}}^{\mathrm{OM}}}$ (Fig. 5), clarifying both the limiting components and spatial extent of subnanometer uncertainty [12,13]. These results emphasize the challenge of calibrating scale factor and propagating its uncertainty in localization microscopy, which is exceedingly rare.

In a final test of the two microscopy methods, we measure the diagonal distance between two corner apertures [Figs. 2(a) and 2(c)], neglecting the common uncertainty of scale factor to isolate other components of uncertainty. For atomic-force microscopy, assuming that the array axes are orthogonal, and that off-axis effects of fabrication precision are negligible, summation of distances between the intermediate 22 aperture pairs [Fig. 2(a)] yields a diagonal distance of 77,792.76 nm ± 1.94 nm. Random effects dominate this uncertainty. For optical microscopy, direct localization of just the two corner apertures [Fig. 2(c)] yields a diagonal distance of 77,792.36 nm ± 0.82 nm. Systematic effects dominate this uncertainty. Thus, the critical dimensions are in subnanometer agreement, validating axis orthogonality for atomic-force microscopy and the accuracy of localization analysis for optical microscopy. Moreover, these results show that optical localization yields half the uncertainty from components that are not common to both microscopy methods, and higher throughput by a factor of 10^5.

This high throughput yields a new capability for fabrication process metrology, enabling critical-dimension localization microscopy of five aperture arrays and three silicon pillar arrays as working standards (Table S5). The silicon pillar arrays

Table 1. Terms and Symbols[abcde]

Term	Symbol
General distance analysis	
True distance between two points	Δ
Experimental measurement of distance between two points by AFM or OM	D^{AFM}, D^{OM}
Experimental measurement of distance between two points in the x or y direction by OM	$D_{\mathrm{x}}^{\mathrm{OM}}$, $D_{\mathrm{y}}^{\mathrm{OM}}$
Uncertainty of D^{OM}	$u_{D^{\mathrm{OM}}}$
Uncertainty of $D_{\mathrm{x}}^{\mathrm{OM}}$ or $D_{\mathrm{y}}^{\mathrm{OM}}$ between one localization result and a reference position	$u_{D_{\mathrm{x}}^{\mathrm{OM}}}$, $u_{D_{\mathrm{y}}^{\mathrm{OM}}}$
Uncertainty of $D_{\mathrm{x}}^{\mathrm{OM}}$ or $D_{\mathrm{y}}^{\mathrm{OM}}$ between two localization results	$u^{\mathrm{II}}_{D_{\mathrm{x}}^{\mathrm{OM}}}$, $u^{\mathrm{II}}_{D_{\mathrm{y}}^{\mathrm{OM}}}$
Scale factor for OM	S
Scale factor uncertainty for OM	σ_S
Scale factor error for OM	ϵ_S
Aperture pair analysis	
Aperture pair index	i
Replicate measurement index	j
Number of replicate measurements of aperture pair distance by AFM	$n_{D^{\mathrm{AFM}}}$
Experimental measurement of aperture pair distance by AFM	$D_{ij}^{\mathrm{AFM}} = \Delta_i + d_{ij}^{\mathrm{AFM}} + \delta_i^{\mathrm{AFM}}$
Random error of distance that is observable between replicate measurements for AFM	d_{ij}^{AFM}
Variance of d_{ij}^{AFM} assuming the same for each aperture pair and replicate measurement, and dividing by $n_{D^{\mathrm{AFM}}}$	$\sigma^2_{d^{\mathrm{AFM}}}/n_{D^{\mathrm{AFM}}}$
Random error of distance that is unobservable between replicate measurements for AFM	δ_i^{AFM}
Variance of δ_i^{AFM} assuming the same for each aperture pair	$\sigma^2_{\delta^{\mathrm{AFM}}}$
Variance of D^{AFM}	$\sigma^2_{D^{\mathrm{AFM}}} = \sigma^2_{\delta^{\mathrm{AFM}}} + \sigma^2_{d^{\mathrm{AFM}}}/n_{D^{\mathrm{AFM}}}$
Number of replicate measurements of aperture pair distance by OM	$n_{D^{\mathrm{OM}}}$
Experimental measurement of aperture pair distance by OM	$D_{ij}^{\mathrm{OM}} = \Delta_i + d_{ij}^{\mathrm{OM}} + \delta_i^{\mathrm{OM}}$
Random error of distance that is observable between replicate measurements for OM	d_{ij}^{OM}
Variance of d_{ij}^{OM} assuming the same for each aperture pair and replicate measurement, and dividing by $\mathrm{n}_{\mathrm{D^{OM}}}$	$\sigma^2_{d^{\mathrm{OM}}}/n_{D^{\mathrm{OM}}}$
Random error of distance that is unobservable between replicate measurements for OM	δ_i^{OM}
Variance of δ_i^{OM} assuming the same for each aperture pair	$\sigma^2_{\delta^{\mathrm{OM}}}$
Variance of D^{OM}	$\sigma^2_{D^{\mathrm{OM}}} = \sigma^2_{\delta^{\mathrm{OM}}} + \sigma^2_{d^{\mathrm{OM}}}/n_{D^{\mathrm{OM}}}$
Distance deviation after averaging over replicate measurements	$D_{i\cdot}^{\mathrm{OM}} - D_{i\cdot}^{\mathrm{AFM}}$
Variance of distance deviations over aperture pairs	$\sigma^2_{D^{\mathrm{OM}}-D^{\mathrm{AFM}}}$

[a] AFM is atomic-force microscopy. OM is optical microscopy.
[b] For clarity, we include only symbols that appear in this study. For example, $D_{\mathrm{x}}^{\mathrm{AFM}}$ does not appear.
[c] For completeness, $u_{D_{\mathrm{x}}^{\mathrm{OM}}} = u^{\mathrm{I}}_{D_{\mathrm{x}}^{\mathrm{OM}}}$ and $u_{D_{\mathrm{y}}^{\mathrm{OM}}} = u^{\mathrm{I}}_{D_{\mathrm{y}}^{\mathrm{OM}}}$, which we revisit in Note S3. For clarity, we simplify this notation in the text.
[d] A dot symbol for j in a subscript denotes an average over replicate measurements.
[e] Additional information and discussions of these quantities are in Table S3 and Notes S2 and S3.

have advantageous material properties as cryogenic microscopy standards in the following application. A statistical meta-analysis [55] yields a consensus mean pitch of 4999.80 nm ± 0.98 nm, an estimate of pitch variability from fabrication corresponding to a standard deviation of 2.70 nm, and a 68% prediction interval for the fabrication of additional working standards ranging from 4997.42 nm to 5002.13 nm (Note S4). These traceable results validate the subnanometer accuracy of mean pitch and, due to the deliberate variation of process parameters, provide a conservative estimate of the reliability of producing replicate standards by electron-beam lithography. This result is an important step toward establishing statistical process control for fabricating and integrating working standards into processes and devices, potentially without additional characterization. However, process variability may exceed scale factor uncertainty, and does so by a factor of five in the present study. Therefore, characterizing individual working standards to minimize this source of variability may be necessary for the most demanding applications.

Applying our methods [Fig. 1(b)], we introduce the comprehensive calibration of a cryogenic microscope—an optical microscope with the sample and objective lens inside a cryostat, and custom optics outside the cryostat (Note S5). Such a

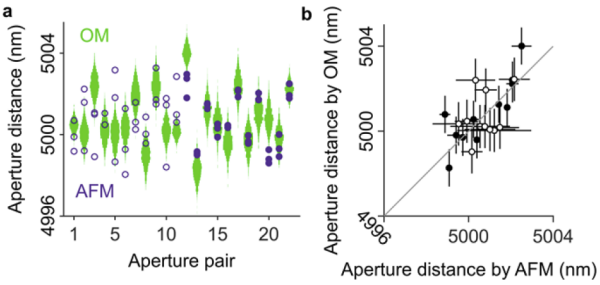

Fig. 4. Aperture distance measurements. (a) Plot showing the correlation of aperture distances from (purple circles) atomic-force microscopy (AFM, hollow circles are axis 1, solid circles are axis 2) and (green violin histograms) optical microscopy (OM). (b) Plot showing the correlation of distances for the different measurements, with a reduction of the data in (a) to mean values and 68% coverage intervals in (b).

Table 2. Distance Uncertainty Evaluation[a]

Uncertainty Component	Evaluation	Absolute Value for x Direction (nm)	Absolute Value for y Direction (nm)
$\sigma_{D^{OM}-D^{AFM}}$	Type A, measurement	0.88 ± 0.21	1.10 ± 0.26
$\sigma_{d^{AFM}}/\sqrt{n_{D^{AFM}}}$	Type A, measurement	0.19 ± 0.05	0.79 ± 0.19
$\sigma_{\delta^{AFM}}$	Type B, estimate	0.02	0.004
$\sigma_{d^{OM}}/\sqrt{n_{D^{OM}}}$	Type A, measurement	0.017 ± 0.004	0.017 ± 0.004
$\sigma_{\delta^{OM}}$	Type A, Eq. (3)	0.86 ± 0.21	0.77 ± 0.32
$\sigma_{\delta^{OM}}$	Type A, [13]	0.88 ± 0.28	1.02 ± 0.27

[a]The solution for $\sigma_{\delta^{OM}}$ depends on a Type B evaluation of $\sigma_{\delta^{AFM}}$, which typically results in an overall categorization of a Type B evaluation for $\sigma_{\delta^{OM}}$. However, the effect of $\sigma_{\delta^{AFM}}$ is negligible, so that the solution for $\sigma_{\delta^{OM}}$ effectively involves only Type A evaluations of the other components, resulting in an effective overall categorization of Type A.

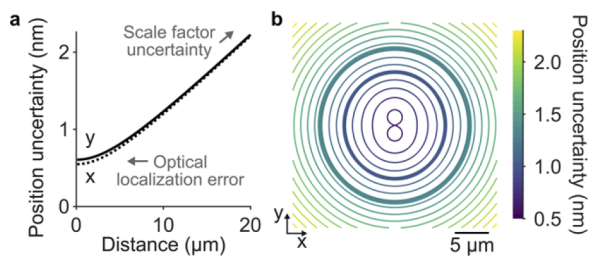

Fig. 5. Traceable position uncertainty. (a) Plot showing position uncertainty of optical microscopy $u_{D^{OM}_{x,y}}$ as a function of distance $D^{OM}_{x,y}$ from a reference point for the (solid) x and (dash) y directions. (b) Contour plot showing the corresponding uncertainty field for position relative to the field center. Two bold contours are limits of (inner) maximum and (outer) mean uncertainty of less than ± 1.0 nm. Contour intervals are 0.1 nm.

system is necessary for the operation and measurement of quantum emitters and is, therefore, central to the integration process [Fig. 1(a)]. Yet, the system optics result in systematic effects that are highly problematic. Our calibration reveals not only unpredictable position errors due to complex optical distortion, but also other errors that previous studies had overlooked, including thermal deviations of reference dimensions and unknown pitfalls of sparsely sampling the imaging field.

To create novel working standards that are suitable for the imaging mode of this microscope system, and that have reliable reference data for coefficient of thermal expansion [58], we pattern submicrometer pillars in a silicon (100) substrate by electron-beam lithography at approximately 293 K, yielding micropillar arrays with a nominal pitch of 5000 nm (Fig. S3, Note S5). Elemental silicon is an excellent reference material for this purpose. Whereas a fused silica or borosilicate substrate, such as a microscope coverslip, would present questions about the type and purity of the glass [59], silicon (100) wafers are widely available and readily amenable to standard lithographic processes. We characterize the pitch of each array by critical-dimension localization microscopy at approximately 293 K, finding a mean pitch across three arrays of 5001.71 nm ± 0.54 nm (Note S5, Table S6). Using reference data for silicon (100) from a study involving cryogenic interferometry [58], we estimate a net contraction of pitch of 0.021509% ± 0.000003%, or 1.07580 nm ± 0.00015 nm, upon cooling to approximately 1.8 K. Importantly, other semiconductor materials that are relevant for photonic integration contract much more and have reference data that are much less certain. For example, gallium arsenide contracts by nearly four times as much [60], presenting both challenges and opportunities that we revisit. For our purposes, the coefficient of thermal expansion for silicon (100) is negligible below approximately 20 K, so we neglect any temperature deviations in this range.

The comprehensive calibration of a cryogenic microscope reveals sources of error that are more complex and less evident than those of a conventional microscope, illuminating potential dark uncertainty in previous studies [55]. To study these effects, we load the reference arrays into the cryostat and record optical micrographs at a peak wavelength of 940 nm near best focus at sample temperatures of approximately 293 K and 1.8 K. We localize the pillars and calibrate the imaging field at each temperature (Note S5), yielding image pixel sizes (Fig. S4) and maps of position errors (Figs. 6 and S5).

Scale factor errors can be significant even for conventional microscopes [Fig. 3(b)] [13], and our study reveals latent sources of such errors for microscope systems with sample cryostats and custom optics. Custom imaging systems may lack a reliable scale factor. Accordingly, previous studies [6,7,22,23] have used fiducial structures of a frame type fabricated by electron-beam lithography for a cryogenic calibration of magnification by a measurement of the distance between two reference positions that span the imaging field. In addition to the questionable assumption of the accuracy of a lithography system to set a reference distance, we find that such measurements yield only a sparse sampling of the complex effects of optical distortion, among other aberrations, that vary at the scale of one to ten wavelengths. These effects can lead to large errors of scale factor [Fig. S6(a)], elucidating a nonobvious but critical problem with a traditional two-point calibration of scale factor. Moreover, previous disregard of the contraction of gallium arsenide substrates at cryogenic temperatures [60] resulted in scale factor deviation that limited the accuracy of these studies [Fig. S6(b)]. These sources of error can significantly degrade the yield of photonic integration [Fig. 1(a)], as we show subsequently.

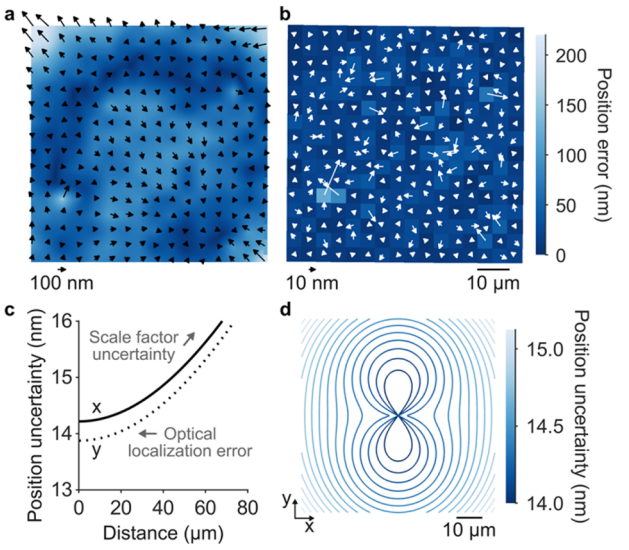

Fig. 6. Cryogenic localization calibration. (a),(b) Vector plots and color maps showing position errors (a) before and (b) after correction for imaging at a temperature of approximately 1.8 K. (c) Plot showing traceable position uncertainty as a function of distance from a reference point for the (solid) x and (dash) y directions. (d) Contour plot showing the corresponding uncertainty field for position relative to the field center.

Separately from the calibration of mean magnification, we observe position errors resulting from optical distortion (Figs. 6 and S5). The spatial variation of these position errors is more complex than that of a conventional microscope [13,27], implying the contributions of both objective lenses and custom optics, and emphasizing the utility of our methods to identify and correct such effects. A supplemental microscope with an alternate placement of an objective lens within a sample cryostat [23] shows even larger position errors (Fig. S7), indicating a general need to calibrate such systems. Complex optical distortion causes position errors as large as 170 nm, with root-mean-square values of 50 nm in x and 55 nm in y for a representative pillar array, dominating an empirical localization precision of less than 2.0 nm (Table S7). Our correction reduces the position errors by more than a factor of three, and the improvement can be larger for different microscopes (Fig. S7) and wider fields [13,15]. We separately measure some components of the total position errors and estimate others to quantitate optical localization errors of 14.2 nm in x and 13.9 nm in y (Fig. 6, Note S5, Table S7). In applying the scale factor calibration and optical distortion correction, additional sources of error increase uncertainty. These include random effects such as photon shot noise, as well as systematic effects such as variation of axial [13,15] and lateral position, which alter apparent position errors, as we discuss subsequently. These additional sources of error become evident upon applying the calibration from images of one array to those of a different array (Table S8).

The calibration results show a distinct hierarchy of optical localization error and scale factor uncertainty for a cryogenic microscope with custom optics, which is evidently more susceptible than a conventional microscope to aberration effects from component misalignments. Optical localization errors of approximately 14 nm are the dominant source of uncertainty across the entire imaging field, whereas scale factor uncertainty results in a position uncertainty that varies from 0 nm at the field center to less than 6 nm at the field periphery (Fig. 6). This hierarchy is due to significant lateral variation of optical localization errors at the micrometer scale, which vary with lower spatial frequency in our conventional microscope, and which Zernike polynomial models can only partially capture. In contrast, interpolant models can fully capture optical localization errors at the pillar locations, but sampling still limits efficacy, resulting in little improvement (Note S5, Table S8). While future work can improve upon these results with denser sampling of the imaging field, the present calibration significantly improves localization accuracy across a wide field and enables a dramatic improvement of registration accuracy.

Following calibration to improve accuracy and establish traceability, the integration process requires the correspondence of microscopy coordinates with the lithographic design. In practice, this involves measurement of fiducial positions around a field of quantum dots. The sequential imaging of fiducial pillars, for example, and quantum dots enables localization and calibration of their relative positions, neglecting any other errors. The correspondence of traceable and nominal positions of fiducials determines a coordinate transformation to map positions in the microscope coordinate system onto the lithographic design. Applying this transformation to the quantum dot positions determines the locations for lithographic placement of photonic structures. The mapping accuracy has a lower bound of the centroid precision of multiple fiducials, which improves as the inverse square root of the fiducial count [61]. In the present calibration, single pillars have a total position error ranging from 13 nm to 19 nm (Table S7), including the effect of photon shot noise. Accordingly, analysis of tens of fiducials reduces the coordinate transformation uncertainty to a negligibly small value. This novel application of our calibration methods enables a significant improvement in process yield, as follows.

To assess the theoretical yield of integrating quantum emitters with photonic structures, we introduce a comprehensive model of registration errors (Note S6, Fig. S8). Such a model is generally informative for accurately integrating quantum emitters and photonic structures of different types and for operation at various wavelengths [6,7,24,29,30,36]. In a specific example, we consider Purcell factor as a performance metric that quantifies the radiative rate enhancement of a quantum dot [62] in a bullseye resonator [6]. This enhancement depends on electric field strength, which varies significantly over a scale of tens of nanometers in typical device geometries. To obtain a representative dependence of Purcell factor on registration error, we interpolate the simulation results from Fig. 6e of [6] for a dipole emitter within a bullseye resonator, with a wavelength of 948.02 nm and azimuthal angles of 0 rad, $\pi/4$ rad, and $\pi/2$ rad (Fig. S9) [6]. Our model results in Purcell factor histograms at each position in the imaging field (Fig. S10), which we reduce to mean values, standard deviations, and mean to standard deviation ratios, or inverse coefficients of variation (Figs. 7 and S11). Large mean values indicate high performance whereas small standard deviations indicate high reliability, so that the inverse coefficient of variation provides an overall measure of performance and reliability. Practical limitations of the calibrations, divergence of reflection and scattering from reference structures and emission from quantum dots [24] at different wavelengths [6,7,22,23], and deviation of the Purcell factor dependence between simulations and experiments, such as from

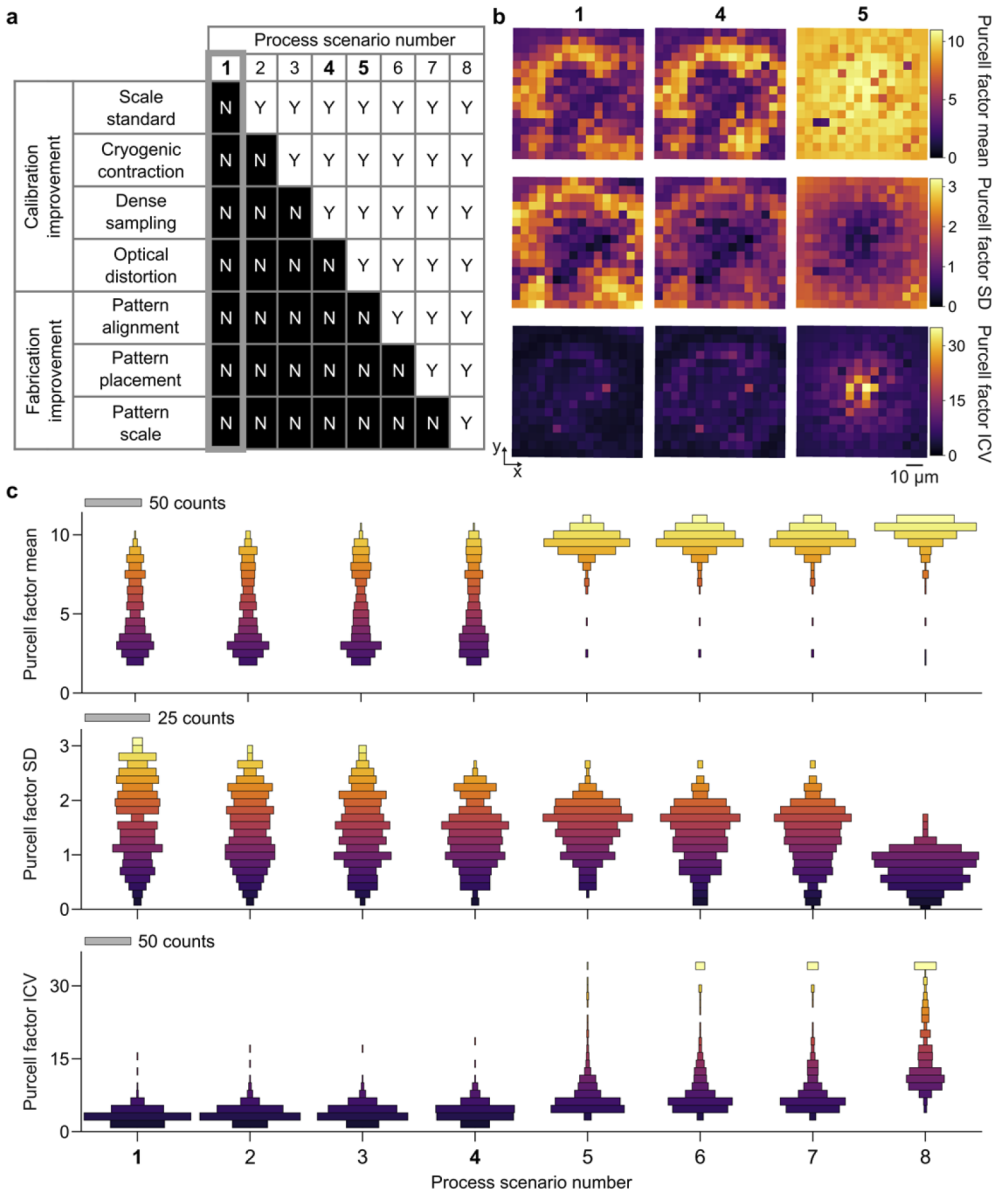

Fig. 7. Purcell factor improvement. (a) Table showing combinations of calibration and fabrication improvements comprising eight process scenarios. (b) Plots showing (top) Purcell factor mean, (middle) Purcell factor standard deviation (SD), and (bottom) Purcell factor inverse coefficient of variation (ICV) across the imaging field for Scenarios 1 (left), 4 (middle), and 5 (right), and a dipole angle of $\pi/4$ rad. (c) Plots showing histograms of (top) Purcell factor mean, (middle) Purcell factor standard deviation, and (bottom) Purcell factor inverse coefficient of variation for each process scenario and a dipole angle of $\pi/4$ rad.

spectral detuning [6], all motivate future work to test and build on our foundational model.

Our process model enables a systematic study of the theoretical effects of microscope calibration and device fabrication on Purcell factor through sequential reductions of registration error, decoupling the previously coupled problem and elucidating previously unrecognized effects. Beginning with the state of the art [6,7,22,23] (Fig. 7, Scenario 1), our process model reduces registration errors from localization measurements, consistent with implementation of our calibration methods, defining five process scenarios. Our process model then reduces registration errors from the process of fabricating photonic structures to elucidate the effects, although such a reduction in fabrication error is purely theoretical in our study, defining three additional process scenarios. A tabular summary of these process scenarios is in Fig. 7(a). Before considering Purcell factor, in combination with Fig. 6, Fig. S8 shows the reduction of registration errors. Maps of the mean, standard deviation, and inverse coefficient of variation of Purcell factor for a representative azimuthal angle of $\pi/4$ rad are in Fig. 7(b). Histograms of these metrics for each process scenario are in Fig. 7(c). Mean Purcell factors for additional dipole angles of 0 rad and $\pi/2$ rad are in Fig. S11. Further details of errors and uncertainties, probability distributions, and data reduction are in Note S6, Table S9, and Figs. S8 and S10.

The state of the art in the scientific literature corresponds in some approximation to Scenario 1, prior to comprehensive calibration of the cryogenic microscope and potential improvement of the fabrication process [Fig. 7(a)]. The mean and standard

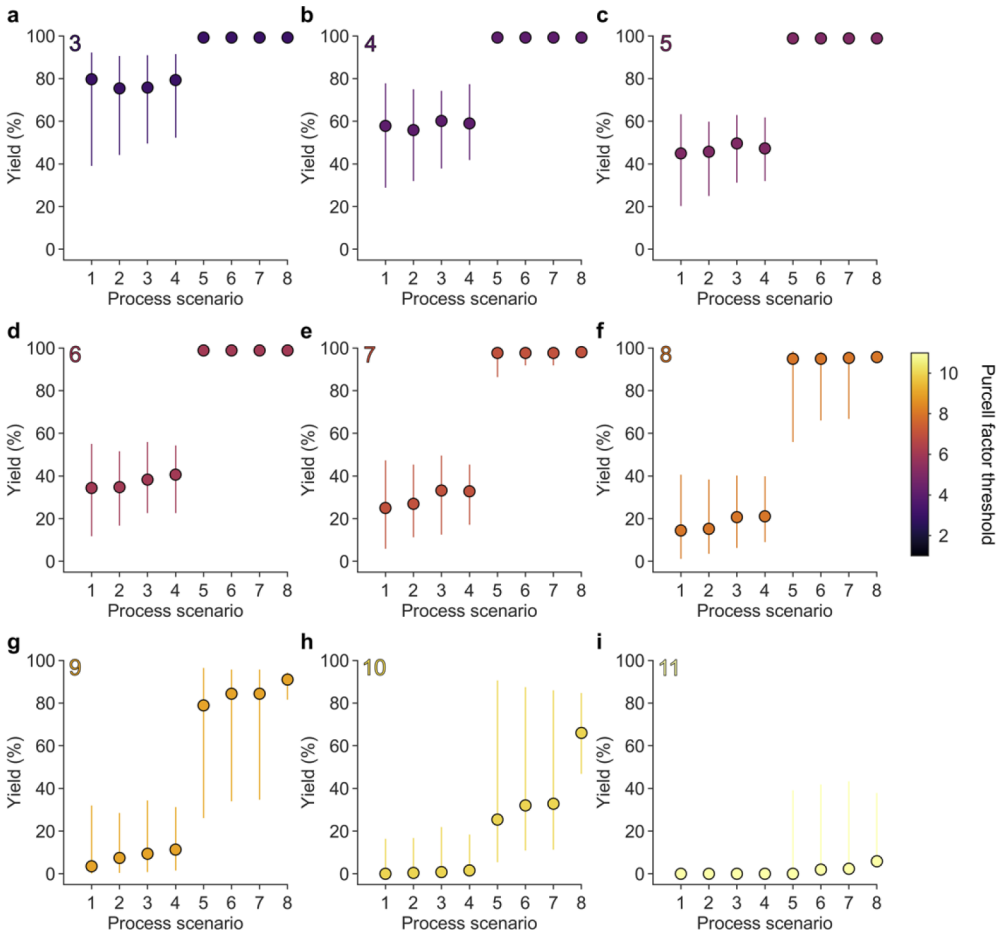

Fig. 8. Process yield trends. (a)–(i) Plots showing theoretical yield for each process scenario for a dipole angle of π/4 rad. The color scale and values in the upper left of each plot indicate the minimum value of Purcell factor that is tolerable. Data are representative and correspond to the mean value of Purcell factor for each field position (Figs. 7 and S10). Vertical bars are 68% coverage intervals and correspond to yields resulting from the 16th and 84th percentile values of Purcell factor for each field position. An alternate presentation of these data is in Fig. S12.

deviation of Purcell factor show complex variation with high frequency across the imaging field [Fig. 7(b)], resulting in broad distributions of both metrics [Fig. 7(c)]. Notably, the mean Purcell factor can vary across nearly its full range within only a few micrometers [Figs. 7(b) and S10], while similar spatial variation and relatively high values of the standard deviation of Purcell factor indicate a highly variable process. The inverse coefficient of variation combines these two metrics, quantifying an unreliable process that still allows for the fortunate fabrication of a few devices demonstrating high performance. This low yield leaves ample room for improvement, as follows.

The effects of microscope calibration are evident in Scenarios 2 through 5. For setting the scale factor, these effects include calibrating a scale standard rather than assuming its nominal dimensions (Fig. 7, Scenario 2), accounting for the net contraction of the standard at cryogenic temperatures rather than neglecting this material property (Fig. 7, Scenario 3), and using an array standard that densely samples the imaging field rather than using alignment marks that provide only a sparse sampling (Fig. 7, Scenario 4). These calibrations provide modest improvements relative to the optical distortion correction (Figs. 7 and S8). However, a larger imaging field is desirable to increase throughput and would increase the effects of scale factor deviation, which would increase registration errors and decrease device performance. The final calibration step is the optical distortion correction, greatly improving both the magnitude and uniformity of the mean Purcell factor near its maximum value across the imaging field (Fig. 7, Scenario 5). The inverse coefficient of variation reaches its peak value near the field center and shows radially decreasing performance and reliability, which is consistent with the increasing effect of scale factor uncertainty.

The effects of registration errors from the fabrication of photonic structures by electron-beam lithography are evident in Scenarios 6 through 8. These include errors of overlay or alignment, feature placement, and scale factor. Removing these sources of error significantly improves performance and reliability across the imaging field, as Fig. 7(c) shows, motivating future work. These results also indicate that the deterministic fabrication of quantum emitters using lithographic systems that yield imperfect placement would still require emitter localization for optimum integration [25,31,32,35]. After characterization, emitter arrays could eliminate any potential divergence of measurement conditions between calibration and experiment.

Completing the extraction of information from the model, we explore the theoretical yield as a function of process scenario number and a threshold for Purcell factor (Figs. 8 and S12). The results show an overall improvement of theoretical yield throughout the process scenarios, with the largest effect due to the optical distortion correction. Small decreases in yield for Scenarios 1 through 4 can occur for lower values of Purcell factor and are due to a partial cancellation of scale factor errors and optical distortion errors. Such an interaction of major effects is interesting, difficult to predict, and an unreliable approach to improve yield. Decreasing scale factor errors from Scenarios 1 through 4 result in narrower coverage intervals for yield, improving process reliability [Figs. 8(a)–8(f)]. Depending on the dipole angle and Purcell factor threshold, the improvement due to comprehensive calibration ranges from one to two orders of magnitude (Figs. 8 and S12, Scenarios 1 and 5). The optical distortion correction allows for a high yield that remains nearly constant as the Purcell factor threshold increases to 8, whereas at the state of the art the yield decreases through this threshold range (Fig. S12). Interestingly, achieving high yield for the highest Purcell factor thresholds is challenging even after comprehensive calibration and theoretical removal of fabrication errors (Figs. 8 and S12, Scenario 8). This limit, corresponding to a registration error of less than approximately 20 nm to achieve a Purcell factor greater than 10 (Fig. S9), is due to the variability and resulting scale factor uncertainty and complex optical distortion of the cryogenic microscope (Table S6). These effects are likely due to sample positioning and optical localization errors. These results form a strong foundation for future studies to optimize microscope calibration and process yield.

3. CONCLUSION

We introduce a methodology to accurately integrate quantum emitters and photonic structures with high yield, advancing far beyond the common practice of selecting a small number of fortunate devices from a much larger population, and enabling the statistical characterization and optimal production of quantum information technologies. Our methodology builds on a new foundation of traceable localization, supporting lithographic process characterization and cryogenic microscope calibration. The results reveal a complex coupling of lithography and microscopy errors, elucidating that this popular integration process is fundamentally dependent on array standards and comprehensive calibrations for reliable registration and lateral scale-out. In this way, we identify and solve a widespread but underappreciated problem, with broader implications to other demanding applications of localization microscopy.

Traceability is the foundation for the most reliable registration of absolute position data from microscopy and lithography systems, which depends on unit conversion, error correction, and uncertainty propagation. To address these issues, we create a master standard that is specifically fit for the purpose of localization microscopy, leading to a corresponding uncertainty field. This new concept elucidates the true limits of uncertainty amid overly optimistic claims of accuracy, shifting the paradigm from the usual focus on localization precision [13] to a broader understanding of total uncertainty. The effects of optical localization error and scale factor uncertainty depend on localization precision and field extent, and, for nanometer precision across a wide field, critically limit accuracy. A metrology framework would help to elucidate this parameter space for photonic integration, among other applications.

Our methodology provides field upgrades of ordinary optical microscopes to traceable metrology systems. Applying this novel capability, we characterize the scale factor of multiple working standards, validating subnanometer accuracy on average but revealing distributional deviations of a few nanometers. This subtle but crucial result validates the central tendency of our lithographic process but also calls into question the common assumption of accuracy for individual standards. Mitigating this issue, localization metrology facilitates process control of lithography systems, and a narrower prediction interval than a few nanometers could yield working standards without the need for individual characterization. Through such qualification, lithographic standards that are broadly available can be usefully accurate, whereas traceable standards could be necessary for validation, as well as the most demanding applications.

We develop reference arrays in a reference material to calibrate localization microscopes with sample cryostats and custom optics. The results elucidate scale factor deviation and complex optical distortion as critical problems, and our solutions create new opportunities for cryogenic microscopy. After calibration and in combination with a reference thermometer, a cryogenic microscope could serve as a localization dilatometer to measure the coefficient of thermal expansion of microscale structures and devices, rather than bulk materials. Alternately, after calibration and in combination with a reference material, a cryogenic microscope could function as a localization thermometer at the sample position, rather than elsewhere in the sample cryostat. The coefficient of thermal expansion of gallium arsenide is potentially suitable for localization thermometry, motivating its traceable characterization as a reference material.

Integrating all of these results, we introduce a process model of registration errors that limit quantum performance. In a theoretical application of our process model to the integration of quantum dots and bullseye resonators, we demonstrate the possibility of dramatically improving the Purcell factor and increasing process yield by orders of magnitude. Such a large benefit could motivate future studies to optimize our methodology by maximizing the similarity of calibration and experiment, and to compare experimental device performance and process yield—with and without traceable calibration. Other photonic structures could also benefit, such as broadband waveguides that require registration errors of less than 10 nm to achieve high coupling efficiency [24–26,29,30]. On this basis, we expect our methodology to be a key enabler of the lab-to-fab transition for quantum information technologies.

Funding. NIST Office of Reference Materials; Physical Measurement Laboratory.

Acknowledgments. The authors acknowledge John Kramar, Leonardo Midolo, and Stephan Reitzenstein for insightful reviews and helpful comments, and Muneesh Maheshwari for helpful comments on custom optics.

Disclosures. The authors declare no conflicts of interest.

Data availability. The data supporting the findings of this study are available from the corresponding author upon reasonable request.

Supplemental document. Supporting content is in Supplement 1.

REFERENCES

1. L. Schermelleh, A. Ferrand, T. Huser, *et al.*, "Super-resolution microscopy demystified," Nat. Cell Biol. **21**, 72–84 (2019).
2. L. Möckl and W. Moerner, "Super-resolution microscopy with single molecules in biology and beyond–essentials, current trends, and future challenges," J. Am. Chem. Soc. **142**, 17828–17844 (2020).
3. P. P. Mathai, J. A. Liddle, and S. M. Stavis, "Optical tracking of nanoscale particles in microscale environments," Appl. Phys. Rev. **3**, 1 (2016).
4. M. Baker, "1,500 scientists lift the lid on reproducibility," Nature **533**, 452–454 (2016).
5. K. Prakash, B. Diederich, R. Heintzmann, *et al.*, "Super-resolution microscopy: a brief history and new avenues," Philos. Trans. R. Soc., A **380**, 20210110 (2022).
6. L. Sapienza, M. Davanço, A. Badolato, *et al.*, "Nanoscale optical positioning of single quantum dots for bright and pure single-photon emission," Nat. Commun. **6**, 7833 (2015).
7. H. Wang, Y.-M. He, T.-H. Chung, *et al.*, "Towards optimal single-photon sources from polarized microcavities," Nat. Photonics **13**, 770–775 (2019).
8. S. M. Thon, M. T. Rakher, H. Kim, *et al.*, "Strong coupling through optical positioning of a quantum dot in a photonic crystal cavity," Appl. Phys. Lett. **94**, 111115 (2009).
9. T. Kojima, K. Kojima, T. Asano, *et al.*, "Accurate alignment of a photonic crystal nanocavity with an embedded quantum dot based on optical microscopic photoluminescence imaging," Appl. Phys. Lett. **102**, 011110 (2013).
10. S. Liu, K. Srinivasan, and J. Liu, "Nanoscale positioning approaches for integrating single solid-state quantum emitters with photonic nanostructures," Laser Photonics Rev. **15**, 2100223 (2021).
11. A. Yildiz, J. N. Forkey, S. A. McKinney, *et al.*, "Myosin V walks hand-over-hand: single fluorophore imaging with 1.5-nm localization," Science **300**, 2061–2065 (2003).
12. A. Pertsinidis, Y. Zhang, and S. Chu, "Subnanometre single-molecule localization, registration and distance measurements," Nature **466**, 647–651 (2010).
13. C. R. Copeland, J. Geist, C. D. McGray, *et al.*, "Subnanometer localization accuracy in widefield optical microscopy," Light: Sci. Appl. **7**, 31 (2018).
14. C. R. Copeland, B. R. Ilic, and S. M. Stavis, "Experimental variation of magnification calibration for localization microscopy," in *Frontiers in Optics* (Optical Society of America, 2019), p. FM1C. 3.
15. C. R. Copeland, C. D. McGray, B. Robert Ilic, *et al.*, "Accurate localization microscopy by intrinsic aberration calibration," Nat. Commun. **12**, 3925 (2021).
16. M. Bierbaum, B. D. Leahy, A. A. Alemi, *et al.*, "Light microscopy at maximal precision," Phys. Rev. X **7**, 041007 (2017).
17. T. Yan, C. Richardson, M. Zhang, *et al.*, "Computational correction of spatially-variant optical aberrations in 3D single-molecule localization microscopy," Biophys. J. **116**, 282a (2019).
18. Y. Li, M. Mund, P. Hoess, *et al.*, "Real-time 3D single-molecule localization using experimental point spread functions," Nat. Methods **15**, 367–369 (2018).
19. J. V. Thevathasan, M. Kahnwald, K. Cieśliński, *et al.*, "Nuclear pores as versatile reference standards for quantitative superresolution microscopy," Nat. Methods **16**, 1045–1053 (2019).
20. M. Raab, I. Jusuk, J. Molle, *et al.*, "Using DNA origami nanorulers as traceable distance measurement standards and nanoscopic benchmark structures," Sci. Rep. **8**, 1780 (2018).
21. L. von Diezmann, M. Y. Lee, M. D. Lew, *et al.*, "Correcting field-dependent aberrations with nanoscale accuracy in three-dimensional single-molecule localization microscopy," Optica **2**, 985–993 (2015).
22. Y.-M. He, J. Liu, S. Maier, *et al.*, "Deterministic implementation of a bright, on-demand single-photon source with near-unity indistinguishability via quantum dot imaging," Optica **4**, 802–808 (2017).
23. J. Liu, M. I. Davanço, L. Sapienza, *et al.*, "Cryogenic photoluminescence imaging system for nanoscale positioning of single quantum emitters," Rev. Sci. Instrum. **88**, 023116 (2017).
24. T. Pregnolato, X.-L. Chu, T. Schröder, *et al.*, "Deterministic positioning of nanophotonic waveguides around single self-assembled quantum dots," APL Photonics **5**, 086101 (2020).
25. N. H. Wan, T.-J. Lu, K. C. Chen, *et al.*, "Large-scale integration of artificial atoms in hybrid photonic circuits," Nature **583**, 226–231 (2020).
26. A. W. Elshaari, A. Skalli, S. Gyger, *et al.*, "Deterministic integration of hBN emitter in silicon nitride photonic waveguide," Adv. Quantum Technol. **4**, 2100032 (2021).
27. P. Ekberg and L. Mattsson, "Traceable X, Y self-calibration at single nm level of an optical microscope used for coherence scanning interferometry," Meas. Sci. Technol. **29**, 035005 (2018).
28. X. Dai, H. Xie, C. Li, *et al.*, "High-accuracy magnification calibration for a microscope based on an improved discrete Fourier transform," Opt. Eng. **52**, 114102 (2013).
29. C. Papon, Y. Wang, R. Uppu, *et al.*, "Independent operation of two waveguide-integrated single-photon sources," arXiv, arXiv:2210.09826 (2022).
30. P. Mrowiński, P. Schnauber, P. Gutsche, *et al.*, "Directional emission of a deterministically fabricated quantum dot–Bragg reflection multimode waveguide system," ACS Photonics **6**, 2231–2237 (2019).
31. J. Wang, Y. Zhou, X. Zhang, *et al.*, "Efficient generation of an array of single silicon-vacancy defects in silicon carbide," Phys. Rev. Appl. **7**, 064021 (2017).
32. A. Branny, S. Kumar, R. Proux, *et al.*, "Deterministic strain-induced arrays of quantum emitters in a two-dimensional semiconductor," Nat. Commun. **8**, 15053 (2017).
33. J. Donges, M. Schlischka, C.-W. Shih, *et al.*, "Machine learning enhanced in situ electron beam lithography of photonic nanostructures," Nanoscale **14**, 14529–14536 (2022).
34. S. Castelletto, M. Barbiero, M. Charnley, *et al.*, "Imaging with nanometer resolution using optically active defects in silicon carbide," Phys. Rev. Appl. **14**, 034021 (2020).
35. M. Sutula, I. Christen, E. Bersin, *et al.*, "Large-scale optical characterization of solid-state quantum emitters," Nat. Mater. **22**, 1338–1344 (2023).
36. S.-W. Xu, Y.-M. Wei, R.-B. Su, *et al.*, "Bright single-photon sources in the telecom band by deterministically coupling single quantum dots to a hybrid circular Bragg resonator," Photonics Res. **10**, B1–B6 (2022).
37. P. De Boer, J. P. Hoogenboom, and B. N. Giepmans, "Correlated light and electron microscopy: ultrastructure lights up!" Nat. Methods **12**, 503–513 (2015).
38. Y.-W. Chang, S. Chen, E. I. Tocheva, *et al.*, "Correlated cryogenic photoactivated localization microscopy and cryo-electron tomography," Nat. Methods **11**, 737–739 (2014).
39. M. Strnad, J. Elsterová, J. Schrenková, *et al.*, "Correlative cryo-fluorescence and cryo-scanning electron microscopy as a straightforward tool to study host-pathogen interactions," Sci. Rep. **5**, 18029 (2015).
40. C. L. Fonta and B. M. Humbel, "Correlative microscopy," Archives of Biochemistry and Biophysics **581**, 98–110 (2015).
41. B. G. Kopek, G. Shtengel, J. B. Grimm, *et al.*, "Correlative photoactivated localization and scanning electron microscopy," PLoS One **8**, e77209 (2013).
42. M. T. Haring, N. Liv, A. C. Zonnevylle, *et al.*, "Automated sub-5 nm image registration in integrated correlative fluorescence and electron microscopy using cathodoluminescence pointers," Sci. Rep. **7**, 43621 (2017).
43. M. Nahmani, C. Lanahan, D. DeRosier, *et al.*, "High-numerical-aperture cryogenic light microscopy for increased precision of superresolution reconstructions," Proc. Natl. Acad. Sci. U. S. A. **114**, 3832–3836 (2017).
44. S. Weisenburger, B. Jing, A. Renn, *et al.*, "Cryogenic localization of single molecules with angstrom precision," in *Nanoimaging and Nanospectroscopy* (SPIE, 2013), 18–26.
45. T. Furubayashi, K. Ishida, H. Kashida, *et al.*, "Nanometer accuracy in cryogenic far-field localization microscopy of individual molecules," J. Phys. Chem. Lett. **10**, 5841–5846 (2019).
46. K.-T. Liao, A. C. Madison, A. L. Pintar, *et al.*, "A lateral nanoflow assay reveals nanoplastic fluorescence heterogeneity," arXiv, arXiv:2101.03881 (2020).

47. D. T. Nguyen, S. Mun, H. Park, *et al.*, "Super-Resolution Fluorescence Imaging for Semiconductor Nanoscale Metrology and Inspection," Nano Lett. **22**, 10080–10087 (2022).
48. L. Mininni, J. Foucher, and P. Faurie, "Advances in CD-AFM scan algorithm technology enable improved CD metrology," in *Metrology, Inspection, and Process Control for Microlithography XXI* (International Society for Optics and Photonics, 2007), p. 65183O.
49. Y. Martin and H. K. Wickramasinghe, "Method for imaging sidewalls by atomic force microscopy," Appl. Phys. Lett. **64**, 2498–2500 (1994).
50. J. A. Kramar, R. Dixson, and N. G. Orji, "Scanning probe microscope dimensional metrology at NIST," Meas. Sci. Technol. **22**, 024001 (2011).
51. R. Dixson, "Traceable calibration of a critical dimension atomic force microscope," J. Micro/Nanolith. MEMS MOEMS **11**, 011006 (2012).
52. "Evaluation of measurement data - Guide to the expression of uncertainty in measurement (GUM 1995 with minor corrections)," Joint Committee for Guides in Metrology, JCGM 100 (2008).
53. B. N. Taylor and C. E. Kuyatt, "Guidelines for evaluating and expressing the uncertainty of NIST measurement results," NIST Technical Note 1297 (1994).
54. A. Possolo, "Simple guide for evaluating and expressing the uncertainty of NIST measurement results," NIST Technical Note 1900 (2015).
55. A. Koepke, T. Lafarge, A. Possolo, *et al.*, "Consensus building for interlaboratory studies, key comparisons, and meta-analysis," Metrologia **54**, S34–S62 (2017).
56. S. Stoudt, A. Pintar, and A. Possolo, "Uncertainty evaluations from small datasets," Metrologia **58**, 015014 (2021).
57. C. R. Copeland, C. D. McGray, J. Geist, *et al.*, "Aperture arrays for subnanometer calibration of optical microscopes," in *2017 International Conference on Optical MEMS and Nanophotonics (OMN)* (IEEE, 2017), pp. 1–2.
58. T. Middelmann, A. Walkov, G. Bartl, *et al.*, "Thermal expansion coefficient of single-crystal silicon from 7 K to 293 K," Phys. Rev. B **92**, 174113 (2015).
59. G. White, "Thermal expansion of silica at low temperatures," Cryogenics **4**, 2–7 (1964).
60. G. Dieye, S. I. Ahmed, A. C. Wade, *et al.*, "Evaluation of gallium arsenide thermal expansion coefficient by extended X-ray absorption fine structure," WJCMP **09**, 37–46 (2019).
61. C. McGray, C. R. Copeland, S. M. Stavis, *et al.*, "Centroid precision and orientation precision of planar localization microscopy," J. Microsc. **263**, 238–249 (2016).
62. J.-M. Gerard and B. Gayral, "Strong Purcell effect for InAs quantum boxes in three-dimensional solid-state microcavities," J. Lightwave Technol. **17**, 2089–2095 (1999).